

Eastward propagating planetary waves with periods of 1–5 days in the winter Antarctic stratosphere as revealed by MERRA and lidar

Xian Lu,¹ Xinzhao Chu,^{1,2} Tim Fuller-Rowell,^{1,3} Loren Chang,⁴ Weichun Fong,^{1,2} and Zhibin Yu^{1,2}

Received 10 April 2013; revised 9 July 2013; accepted 7 August 2013; published 5 September 2013.

[1] This study presents the first report of planetary wave (PW) influences on significant temperature perturbations (10–20 K) within a course of one day detected by an Fe lidar from 35 to 51 km in the austral winter of 2011 at McMurdo (77.8°S, 166.7°E), Antarctica. Such large temperature perturbations are captured in the Modern Era Retrospective-Analysis for Research and Applications (MERRA) data and correspond to various phases of eastward propagating PWs with periods of 1–5 days as revealed in MERRA. The strongest PW dominating the temperature perturbations has a period of 4–5 days with wavenumber -1 . A 2–day wave with wavenumber -2 and a 1.25–day wave with wavenumber -3 also have significant influences. We find that these eastward propagating PWs are highly confined to winter high latitudes, likely because negative refractive indices equatorward of $\sim 45^\circ\text{S}$ result in evanescent wave characteristics and prevent the PWs from propagating to lower latitudes. The Eliassen-Palm flux divergence and instability analyses suggest that barotropic/baroclinic instability at 50°S – 60°S induced by the stratospheric polar night jet and/or the “double-jet” structure is the most likely wave source. Such instability in the region poleward of 70°S is a complementary source for the 4–day wave, where we find that the heat flux of the 4–day wave is large and transported from $\sim 70^\circ\text{S}$ toward the pole above 40 km. This transport direction is likely linked to the meridional gradient of background temperature. The migrating diurnal tide near 78°S in the upper stratosphere is discernable, but significantly smaller than that of the dominant 4–day wave.

Citation: Lu, X., X. Chu, T. Fuller-Rowell, L. Chang, W. Fong, and Z. Yu (2013), Eastward propagating planetary waves with periods of 1–5 days in the winter Antarctic stratosphere as revealed by MERRA and lidar, *J. Geophys. Res. Atmos.*, 118, 9565–9578, doi:10.1002/jgrd.50717.

1. Introduction

[2] The eastward propagating 4– and 2–day planetary waves (PWs) are ubiquitous in the winter polar stratosphere [Manney and Randel, 1993; Allen *et al.*, 1997; Coy *et al.*, 2003]. The 4–day wave with wavenumber -1 (negative wavenumber refers to eastward propagating) was first computed from the satellite radiance measurements by Venne and Stanford [1979]. A 2–day wave with wavenumber -2 has also been observed and appears to be phase locked to the 4–day wave in brightness temperatures in the winter polar

stratosphere [Prata, 1984]. In addition, a 1.2–day wave with wavenumber -3 and 0.8–day wave with wavenumber -4 have also been found and move with the same phase speeds as the 2– and 4–day waves [Lait and Stanford, 1988]. Together, these PWs move eastward forming a quasi-nondispersive wave packet and largely consist of the ubiquitous and long-lasting (more than one month) “warm pool” phenomenon that circles around the winter pole in the stratosphere [Prata, 1984; Allen *et al.*, 1997; Lait and Stanford, 1988].

[3] This series of eastward propagating PWs has great impacts on the thermal and dynamical structures of the polar stratosphere, e.g., they result in remarkable wind, temperature and constituent variabilities of the polar stratosphere with a period of 4–5 days [Allen *et al.*, 1997; Coy *et al.*, 2003]; the 4–day wave is responsible for the main motion of the polar vortex at its upper levels [Manney *et al.*, 1998]. They can also affect the horizontal transport and distribution of species such as O_3 , H_2O , and CH_4 in the polar region [Allen *et al.*, 1997; Manney *et al.*, 1998; Coy *et al.*, 2003]. Meanwhile, these PWs are also prevalent in the winter polar mesosphere and have been observed by ground-based radars and spaceborne satellites [Fraser *et al.*, 1993; Lawrence *et al.*, 1995; Lawrence and Randel, 1996; Palo *et al.*, 1998; Forbes *et al.*,

¹Cooperative Institute for Research in Environmental Sciences, University of Colorado at Boulder, Boulder, Colorado, USA.

²Department of Aerospace Engineering Sciences, University of Colorado at Boulder, Boulder, Colorado, USA.

³Space Weather Prediction Center, NOAA, Boulder, Colorado, USA.

⁴Institute of Space Science, National Central University, Jhongli, Taiwan.

Corresponding author: X. Lu, Cooperative Institute for Research in Environmental Sciences, University of Colorado at Boulder, Box 216 UCB, Boulder, CO 80309-0216, USA. (xian.lu@colorado.edu)

1999; Azeem *et al.*, 2005; Garcia *et al.*, 2005; Merzlyakov and Pancheva, 2007; Baumgaertner *et al.*, 2008]. By using the Microwave Limb Sounder (MLS) measurement, Sandford *et al.* [2008] provided direct evidence that the wintertime 2-day polar wave originates in the stratosphere, indicating that the PWs play crucial roles in dynamical coupling of the atmosphere, and even affect ionospheric variability in the polar region.

[4] Two types of zonal mean flow instabilities have been proposed to be responsible for the generation of these PWs, with one being the barotropic instability of the stratospheric polar night jet and the other one being the barotropic/baroclinic instability of the double-jet structure (i.e., polar night jet and subtropical mesospheric jet). The winter polar night jet is composed of strong eastward zonal mean zonal winds centered near 50°S–60°S in the upper stratosphere and the subtropical mesosphere jet usually locates around 30°S between 50 and 70 km [see Randel and Lait, 1991, Figure 11; Lawrence and Randel, 1996, Figure 5]. The polar night jet instability explains the barotropic structure of the 4-day wave (e.g., no apparent vertical phase tilt) and poleward momentum flux [e.g., Hartmann, 1983; Manney *et al.*, 1988; Manney, 1991], while the double-jet instability accounts for equatorward momentum flux and significant equatorward heat flux [Manney, 1991; Randel and Lait, 1991; Manney and Randel, 1993; Watanabe *et al.*, 2009]. In our study, both instabilities are identified in the winter Southern Hemisphere using Modern Era Retrospective-Analysis for Research and Applications (MERRA) data in 2011, and the direction of the consequent momentum fluxes is consistent with previous studies. However, different from former studies, we find that the heat flux poleward of 70°S caused by the barotropic/baroclinic instability of the double-jet structure is transported toward the pole, rather than the equator. The reason for this discrepancy will be further discussed in section 4.

[5] During the austral winter of 2011, an Fe Boltzmann lidar was operated to collect data over 18 days for a total of 249 h at McMurdo (77.8°S, 166.7°E), Antarctica. It was frequently observed in the winter upper stratosphere and lower mesosphere (~35 to 70 km) that temperature could increase or decrease on the order of 10–20 K within a course of one day. Despite high-resolution and reliable temperature observations by lidar at a single station, its noncontinuous sampling makes it difficult to distinguish tides from PWs with longer periods, regarding both waves could introduce such temperature changes. The continuous global coverage provided by the Modern Era Retrospective-Analysis for Research and Applications (MERRA) data is complementary in this respect and similar temperature increases/decreases have been captured in the MERRA. The goal of this paper is to utilize the valuable opportunity provided by the combination of lidar and MERRA data to identify the dominant causes of the observed temperature changes. As will be shown in section 3, they are mainly caused by the eastward propagating PWs, which are substantially stronger in the Southern Hemisphere (SH) compared to the Northern Hemisphere (NH) and are confined to high latitudes [Venne and Stanford, 1982; Randel and Lait, 1991; Lawrence and Randel, 1996; Sandford *et al.*, 2008]. The reason for this interhemispheric difference probably resides in the massive transience of the background structure associated with Arctic Sudden Stratospheric Warming (SSW) events [Lawrence and Randel, 1996] and weaker polar

vortex due to more frequent encroachment by strong stationary PWs in the NH. Therefore, measurements at such a high southern latitude like McMurdo provide a unique opportunity to assess PW influences on lidar temperature variations, which we believe has not been reported before.

[6] Although prior studies have been dedicated to studying wave characteristics and sources using satellite or National Meteorological Center (NMC) data, most focused on latitudes of 50°S–60°S associated with the polar night jet or the double-jet structure and regard it as the dominant wave source region [Randel and Lait, 1991; Manney and Randel, 1993; Watanabe *et al.*, 2009]. However, our study finds that although this region is essential to generate and/or amplify 2-day and 1.25-day PWs and part of the 4-day PWs, the region poleward of 70°S above 40 km characterized by persistent barotropic/baroclinic instability can be an important complementary source region to the 4-day wave in the austral winter of 2011.

2. Data Sources and Comparison Between MERRA and Lidar Data

2.1. Data Sources

[7] The University of Colorado lidar group deployed an Fe Boltzmann lidar to Arrival Heights (77.83°S, 166.67°E), McMurdo, in December 2010, with support from the United States Antarctic Program and Antarctica New Zealand, and has been collecting data since then [Chu *et al.*, 2011a, 2011b]. This lidar measures temperatures in the mesosphere and lower thermosphere (MLT) using the Fe Boltzmann technique and from 30 to 70 km using the Rayleigh integration technique. The principles, capabilities, and error analysis of the lidar can be found in Chu *et al.* [2002]. The high-precision Fe lidar measurements at McMurdo have led to numerous new scientific insights into polar mesospheric clouds [Chu *et al.*, 2011a], neutral Fe layers and fast gravity waves reaching 155 km in the thermosphere [Chu *et al.*, 2011b], solar effects on the mesospheric Fe layers [Yu *et al.*, 2012], extremely strong and persistent wintertime inertia-gravity waves [Chen *et al.*, 2013], and thermal tides in the winter polar temperatures from 30 to 110 km (W. Fong *et al.*, Winter temperature tides from 30 to 110 km at McMurdo (77.8°S, 166.7°E), Antarctica: Lidar observations and comparisons with WAM, submitted to *Journal of Geophysical Research: Atmospheres*, 2013). Temporal and vertical resolutions of lidar temperatures used in this paper are 1 h and 1 km, respectively. With these resolutions, the Rayleigh temperature error is less than 1 K from 30 to 45 km and up to 2 K around 55 km.

[8] MERRA was developed by NASA's Global Modeling and Assimilation Office for the satellite era using a new version of the Goddard Earth Observing System Data Assimilation System Version 5 (GEOS-5). It has now caught up to the current period and been continued as a near-real-time climate analysis [Rienecker *et al.*, 2011]. The temporal resolution of MERRA data is 3 h and vertical resolution is about 2–3 km. MERRA data have been successfully applied in diverse studies such as the energy budget of the polar atmosphere [Cullather and Bosilovich, 2012], climate variability [Bosilovich, 2013], global thermal tides [Sakazaki *et al.*, 2012], etc. Through incorporating MERRA into the Whole Atmosphere Community Climate Model, which further constrains the stratosphere and mesosphere dynamics of the Thermosphere Ionosphere Mesosphere Electrodynamics-General Circulation Model, the

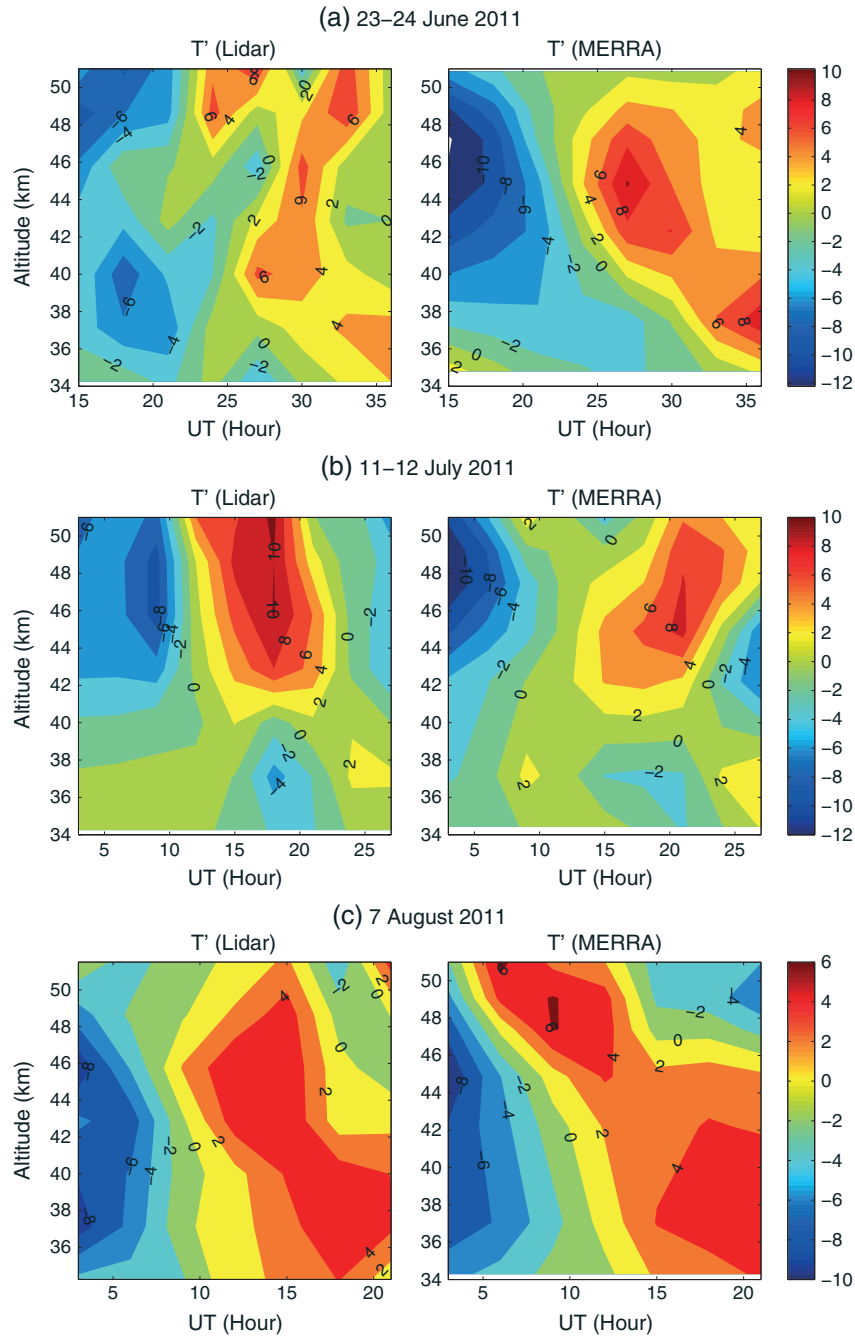


Figure 1. Comparisons of temperature perturbations between lidar measurements at McMurdo (77.8°S, 166.7°E) and MERRA data at (78.1°S, 166.9°E) on (a) 23–24 June, (b) 11–12 July, and (c) 7 August 2011, respectively. The unit is K.

realistic weather patterns embedded in MERRA are found to be the key for reproducing observed day-to-day ionospheric variability [Liu *et al.*, 2013]. These studies all indicate that MERRA data can be used in our study with high fidelity.

[9] Before using the MERRA data in this study, it is of great importance to verify that the temperature change patterns (magnitudes and phases of temperature increases/decreases) measured by the lidar at McMurdo are captured in the MERRA. Here we focus on temperature perturbations between ~35 and 51 km from MERRA and compare them with lidar observations.

2.2. Comparison of Temperature Perturbations Between MERRA and Lidar

[10] Plotted in Figure 1 are the comparisons of temperature perturbations between lidar and MERRA in three different periods of time in the austral winter: 23–24 June, 11–12 July, and 7 August 2011, respectively. The nearest location in MERRA (78.13°S, 166.88°E) to McMurdo is chosen for this comparison. The data set mean temperature for a given period is subtracted to obtain temperature perturbations for both lidar and MERRA data. In order to perform a more consistent comparison, lidar measurements are shown with the

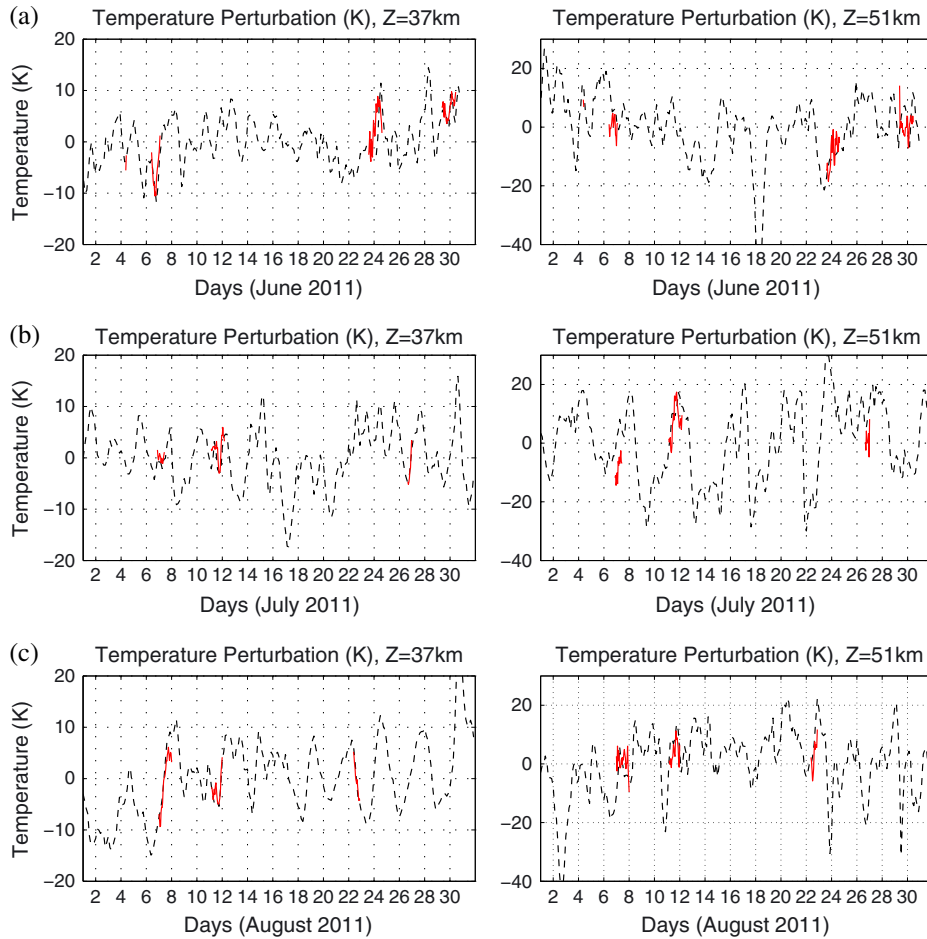


Figure 2. Temperature perturbations in (a) June, (b) July, and (c) August 2011 obtained from MERRA data at (78.1°S, 166.9°E) (black dashed lines) and lidar observations at McMurdo (red lines) at 37 and 51 km, respectively. The unit is K.

same 3 h time steps of MERRA, which are 0, 3, ..., and 21 UT. Similarities between MERRA and lidar observations are obvious in that colder temperatures are found in the beginning of the data sets and they become warmer afterward with regard to the mean temperature for a given period. On 11–12 July 2011 and 7 August 2011, the magnitudes of the temperature increases are also comparable between MERRA and lidar below 48 km. Temperatures increase within a course of one day are 10–18 K at 42–48 km on 11–12 July 2011 and are 10–12 K at 36–48 km on 7 August 2011, respectively. The differences between these two data sets, however, are nonnegligible. For instance, the lidar observations show finer structures and smaller magnitudes of temperature increases than MERRA on 23–24 June, and the warm phase of temperature is shifted by a couple of hours above ~40 km in the MERRA on 11–12 July 2011. Despite the differences, the trends and phases of temperature changes are generally consistent between MERRA and lidar, and MERRA captures the right magnitudes in the cases of July and August.

[11] In order to demonstrate that the reasonable agreement between MERRA and lidar is a general case, all the lidar observations from June to August are compared with MERRA in Figure 2. We subtract the monthly-mean temperatures and show one month temperature perturbations derived from the MERRA data with temporal resolution of

3 h (black dashed lines in Figure 2). Meanwhile, lidar temperature perturbations acquired by subtracting the observational mean for a given month are also plotted with 1 h temporal resolution (red solid lines). Figure 2 reveals that temperature perturbations in MERRA match lidar observations reasonably well in most cases, especially at 37 km. For example, a lidar temperature decrease of ~8 K and then an increase of ~10 K on 7 June 2011 at 37 km are captured in MERRA. The decreasing and then increasing trends also agree well between the two data sets on 11 July at 37 km. At 51 km, lidar temperature first increases for ~20 K and decreases for ~10 K on 11 July, which are also present in MERRA. In some other cases, monotonic temperature variations observed by lidar are well reproduced in the MERRA data, such as 26 July, 7 and 22 August 2011 at 37 km.

[12] In general, inconsistencies tend to be larger near the upper boundary of MERRA in both Figures 1 and 2. In Figure 2, the temperature change trends are quite different between lidar and MERRA on 29–30 June at 51 km, and on 7 July 2011, an offset of ~5 K in temperature perturbations is found although the temperature change trends are similar (right panels in Figures 2a and 2b, respectively). It is likely associated with the fact that IGW amplitudes become larger as altitude increases [Chen *et al.*, 2013] and may not be well resolved by the gravity wave parameterization in MERRA

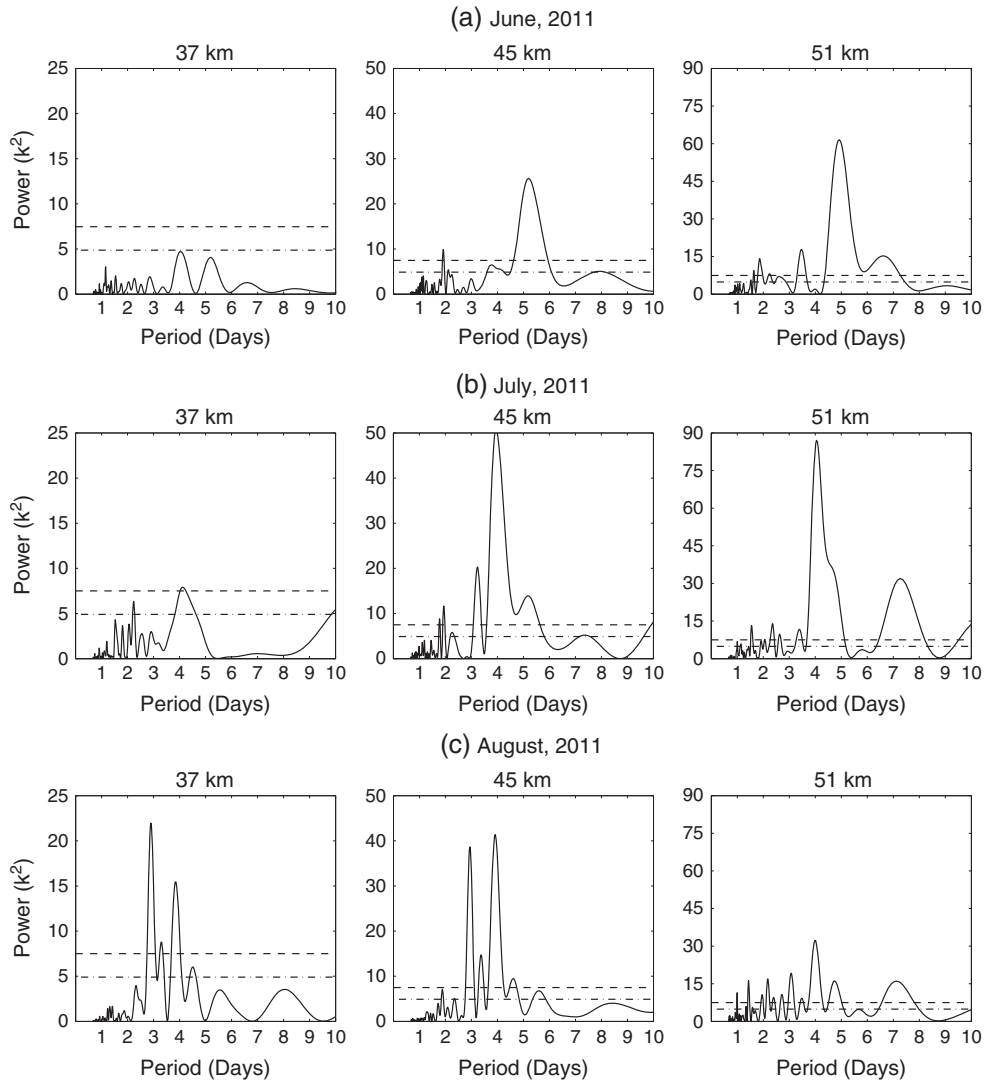


Figure 3. Lomb-Scargle power spectra in (a) June, (b) July, and (c) August at three different altitudes (i.e., 37, 45, and 51 km) computed from the MERRA temperature perturbations at (78.1°S, 166.9°E). Dashed and dash-dotted lines correspond to the 95% and 50% confidence levels, respectively. The unit is K^2 .

near the upper boundary. It is worth to mention that MERRA's time resolution is 3 h, which cannot resolve short-period oscillations caused by GWs shown as the higher-frequency wiggles in lidar observations. Nevertheless, considering that MERRA is a reanalysis data set retrieved from both data assimilation and numerical modeling, it is not expected to match the lidar observations exactly.

[13] According to Figures 1 and 2, temperature perturbations (from trough to ridge) on the order of 10–20 K within one day from 35 to 51 km are resolved in MERRA and their change phases are generally comparable with lidar observations. The reasonable agreement has been reached between lidar and MERRA, indicating that MERRA data are suitable for our study here.

3. Wave Characteristics

[14] From the spacing between the peaks and troughs of the continuous MERRA temperature perturbations, Figure 2 clearly illustrates that PWs with periods of days are mainly responsible for the 10–20 K temperature increases/decreases, rather than

tides. For instance, a temperature increase of ~ 20 K on 11–12 July at 51 km occurs within the duration of a 4 day wave that reaches its peaks around day 8 and day 12, and a temperature increase of ~ 15 K on 7 August 2011 at 37 km is accompanied by a 4-day wave that peaks around day 4 and day 8. A temperature decrease of ~ 10 K on 22 August 2011 is associated with a 2-day wave peaking around days 22 and 24 (Figure 2c, left panel). Similarly, a temperature increase of 10 K on July 27 at 37 km (Figure 2b, left panel) and an increase of 20 K on August 23 at 51 km (Figure 2c, right panel) result from 2-day wave oscillations. A closer inspection reveals that on 11–14 June, 22–26 July, and 10–14 August at 37 km, the adjacent two peaks of temperature perturbations are usually apart from each other by 1 to 2 days, indicating that they are modulated by PWs with periods of $\sim 1 - 2$ days. Overall, the temperature perturbations are modulated by the superposition of these PWs.

3.1. Spectral Analyses and Dominant PW Periods

[15] To determine the dominant PW periods, the Lomb-Scargle (LS) periodogram [Scargle, 1982] is computed from

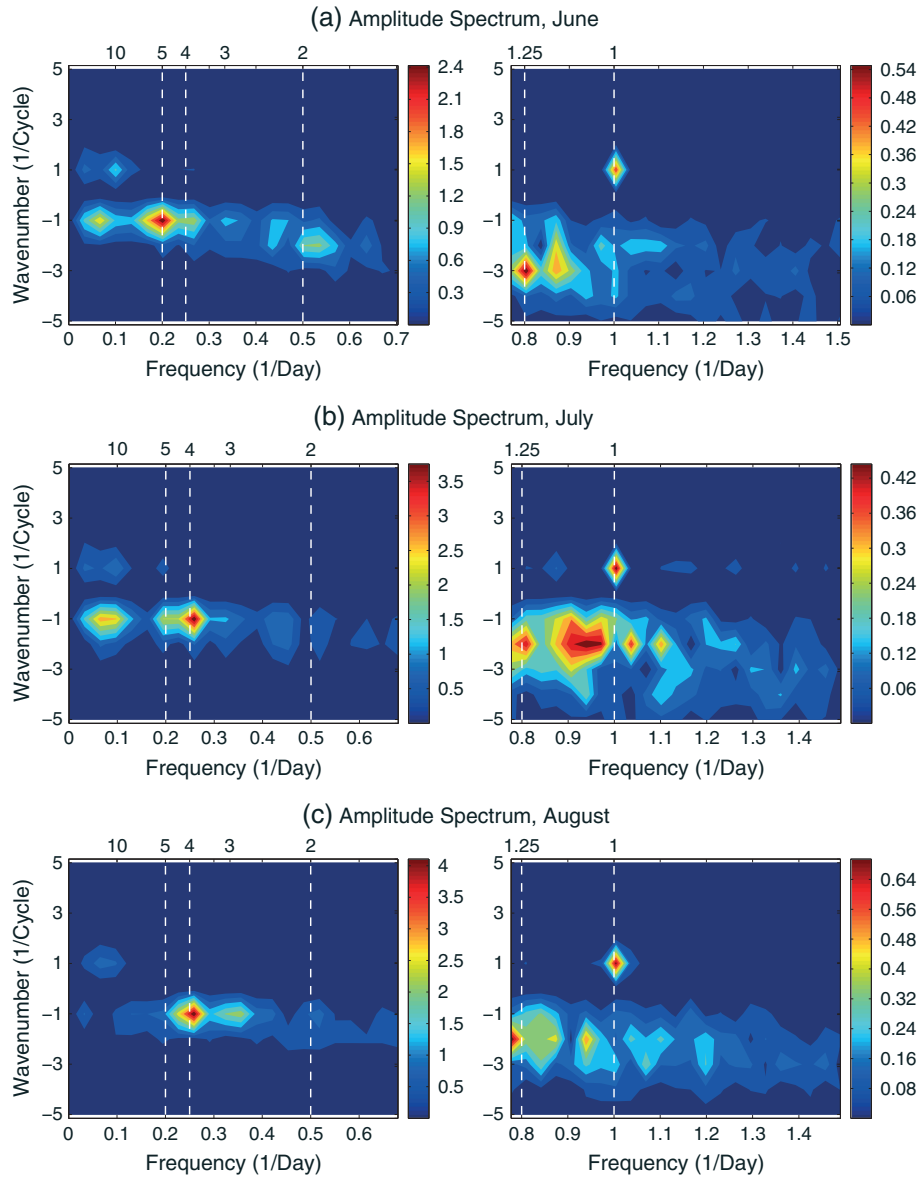


Figure 4. Two-dimensional FFT amplitude spectra averaged from 32 to 51 km for (a) June, (b) July, and (c) August 2011, according to the MERRA temperature perturbations at 78.1°S . Corresponding periods are given on the top axes and white dashed lines highlight periods of 5, 4, 2, 1.25, and 1 days. Positive (negative) wavenumber corresponds to westward (eastward) propagating PW. The unit is K.

the MERRA temperature perturbations (at the nearest location to McMurdo) of each month at three altitudes of 37, 45, and 51 km (Figure 3). Since 51 km is close to the upper boundary, the spectral analysis results should be viewed with caution. A window width of one month is chosen for the LS analysis in order to acquire sufficient resolution in the frequency domain (thus diminishing the aliasing effect) and track spectral variations from month to month. As illustrated in Figure 3, a prominent feature is the dominance of a 5 day PW in June and 4-day PWs in July and August. The largest monthly-mean amplitude of $\sim 9.4\text{K}$ for the 4-day wave is found at 51 km in July. Wave amplitudes increase with altitude from 37 to 51 km in June and July, while decreasing slightly from 45 to 51 km in August. A quasi 3 day wave is also noticeable and attains a significant amplitude in August (peaking around 6K at 45 km). In addition, a quasi-2-day wave is found

above the 95% confidence level at 45 and 51 km in all three winter months, whereas it has a much smaller amplitude than the 4-day wave.

[16] A 2-D fast Fourier transform (FFT) is applied to the MERRA temperature perturbations at 78.1°S (as a function of time and longitude) for each month and each altitude (with a 2–3 km step) to determine both the period and wavenumber of the dominant PWs. Figure 4 reveals the mean amplitude spectra averaged from 32 to 51 km, where PWs maintain significant amplitudes. For the left panels, the frequency domain ranges from 0 to 0.7day^{-1} , covering frequencies of the 4-day and 2-day waves. Since shorter-period PWs (i.e., period around 1 day) tend to have weaker amplitudes, color bars with finer levels and smaller ranges are used for waves with frequencies ranging from 0.75 to 1.5day^{-1} (right panels in Figure 4).

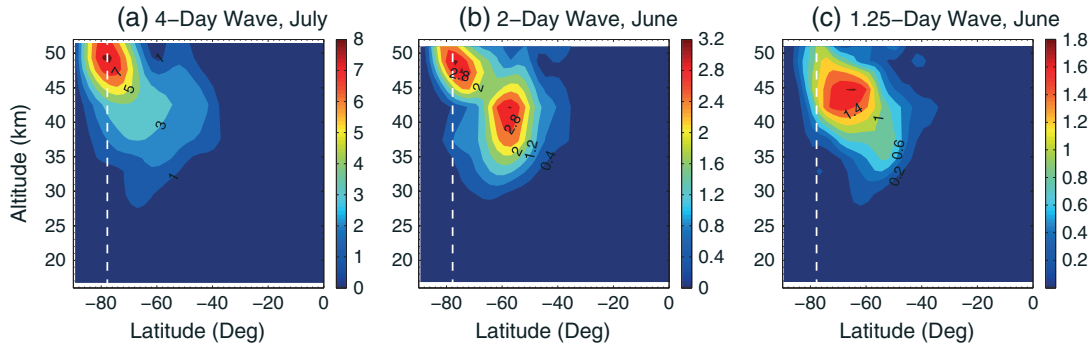


Figure 5. Temperature amplitudes of (a) 4-day PW with wavenumber -1 in July, (b) 2-day PW with wavenumber -2 , and (c) 1.25-day PW with wavenumber -3 in June 2011. The contour intervals are 1, 0.4, and 0.2 K from left to right, respectively. The location of McMurdo is denoted as the white dashed line. The unit is K.

[17] The most dominant 4-day (5-day) wave is eastward propagating with respect to the ground and has wavenumber -1 in the three winter months. Quasi-2-day and 1.25-day PWs also propagate eastward to the ground but their wavenumbers (inversely proportional to phase speeds) vary with month. For the quasi-2-day (quasi-1.25-day) wave, wavenumber -2 (-3) is found in June and it changes to wavenumber -1 (-2) in July and August. Due to the eastward propagations of the 4-, 2-, and 1.25-day PWs and similar generating mechanisms (which will be discussed in section 4), they likely fall into the category of waves associated with the “warm pool phenomenon” in the winter polar stratosphere [Prata, 1984; Allen *et al.*, 1997; Lait and Stanford, 1988]. According to the wavelet spectral analysis (not shown), these three waves are clearly separated by periods and exist simultaneously. It is found from the MERRA data that the phase speeds of these three PWs can be quite different in different months especially for July and August. This indicates the dispersive nature of the wave packet with which they move along in 2011. For 4(5)-, 2-, and 1.25-day waves, the phase speeds are 0.2, 0.25, and 0.27 cycle/d in June and 0.25, 0.5, and 0.4 cycle/d in July and August, respectively. Here a cycle means one complete circle along all longitudes at certain latitude. The discrepancy between the dispersive nature of the wave packet in our study and the nondispersive nature of that reported by Lait and Stanford [1998] using satellite temperatures in 1979 and 1980 suggests that dynamics of the “warm pool” may vary among different years.

[18] The longer-period PWs (>10 days) are also noticeable in Figure 4 (left panels with frequencies smaller than 0.1 day^{-1}). In June and July, the eastward propagating PWs with wavenumber -1 and periods between 10 and 20 days can be identified, which is quite similar to the quasi 10 day waves with wavenumber -1 prior to the midwinter stratospheric warming in the SH in 2002 [Palo *et al.*, 2005]. In their study, it is believed that these eastward propagating quasi 10 day waves are generated by the instability of the zonal mean flow. The waves were found to extend from the lower stratosphere (~ 20 km) into the lower thermosphere (up to ~ 120 km) with small amplitude attenuation as revealed by the temperature observations from the Sounding of the Atmosphere using Broadband Emission Radiometry. In addition to these eastward propagating longer-period PWs, Figure 4 also demonstrates the

quasi 10 day westward propagating (wavenumber = 1) PWs in June and July and a quasi 20 day westward propagating wave (wavenumber = 1) in August.

[19] The migrating diurnal tide (DW1, frequency = 1 day^{-1} and wavenumber = 1) can be identified with monthly-mean amplitudes on the order of $0.5\text{--}0.7 \text{ K}$ at 78°S averaged from 32 to 51 km, which is consistent with the results of Sakazaki *et al.* [2012]. In addition to DW1, two nearly symmetric frequency peaks around 1 day^{-1} are found at ~ 0.95 and $\sim 1.05 \text{ day}^{-1}$ in all months and another two symmetric frequency peaks are found at ~ 0.9 and $\sim 1.1 \text{ day}^{-1}$ in July and August (see right panels of Figure 4). They are all eastward propagating waves with wavenumber -2 and usually weaker than DW1. We conclude that temperature variations at periods around 1 day (Figure 2) are caused by the superposition of multiple waves with periods around 1 day, including but not limited to DW1 and the 1.25-day PW.

3.2. Global Structure of Dominant 4-, 2-, and 1.25-Day PWs

[20] In this paper we focus on studying the 4-day wave with wavenumber -1 in July, 2-day wave with wavenumber -2 , and 1.25-day wave with wavenumber -3 in June, when they reach the maximum amplitudes and are representative of the global structure of these waves. Similar characteristics of these waves in other months are also found but are not shown here. A detailed study on the thermal tides can be found in Fong *et al.* (submitted manuscript, 2013). To derive a global picture of these dominant PWs, we first apply 2-D FFT spectral analysis to the MERRA temperature perturbations along longitude spanning 360° and time spanning a month to get the wave spectra as a function of frequency and wavenumber for each latitude and altitude. The power spectral density corresponding to a dominant PW frequency and wavenumber, e.g., frequency = 0.25 day^{-1} and wavenumber = -1 for the 4-day wave, is then taken to derive the amplitude and phase of this particular PW at this latitude and altitude. Such calculations are applied to the altitude range of 10–51 km at a step of 2–3 km and to the global latitudes at a step of 1.25° . The overall global pictures of the obtained temperature amplitudes of the 4-, 2-, and 1.25-day PWs are illustrated in Figure 5. The 4-day wave structure in July (Figure 5a) is similar to the 5-day wave in June and the 4-day wave in August, so

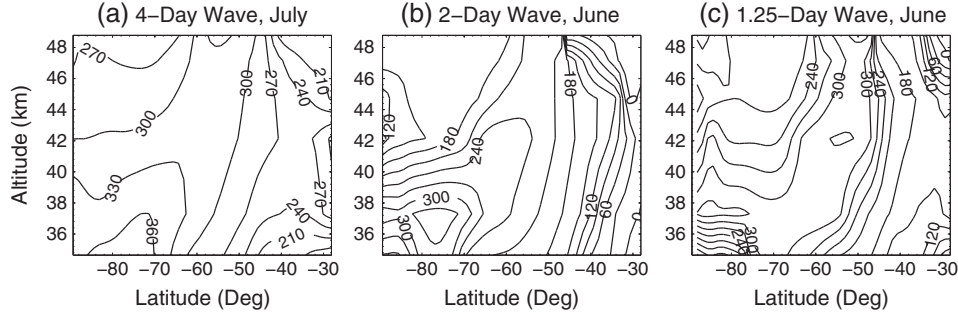


Figure 6. Similar to Figure 5 except for wave phases at an altitude range of ~ 34 – 49 km and latitudes poleward of $\sim 28^\circ$ S. Wave phases are defined as longitudes corresponding to maximum wave amplitudes at 0 UT on 1 June 2011 and 0 UT on 1 July 2011. Contour interval is 30° . The unit is degree.

these two waves are not shown. Consistent with previous studies, all the three PWs are confined to the SH polar region in the austral winter and are barely seen in the NH, which is therefore omitted from Figure 5.

[21] Figure 5 clearly shows that the PWs increase to significant amplitudes above 30 km with maximum monthly-mean amplitudes of 8, 3.2, and 1.8 K for 4–, 2–, and 1.25–day waves, respectively. Concerning the latitudinal distribution, the 4–day wave peaks at 70° S– 80° S, 1.25–day wave peaks at 60° S– 70° S, whereas 2–day wave has two peaks at 70° S– 80° S and 50° S– 60° S, respectively. The 77.83° S latitude of McMurdo makes it an ideal site for observing the 4– and 2–day waves (see white dashed lines in Figure 5). This also explains why the winter stratosphere temperatures are significantly modulated by these PWs as observed by the lidar at McMurdo. Both the horizontal propagation direction and latitudinal structure of these eastward propagating 5–, 4–, and 2–day waves are distinct from those of the normal modes with the same periods. The normal modes of 5– and 4–day waves are the symmetric westward propagating modes with wavenumbers 1 and 2, respectively, and that of the 2–day wave is the asymmetric westward propagating mode with wavenumber 3 [Forbes, 1995]. The apparent differences of the resolved eastward propagating PWs from the normal modes and their confinement to southern high latitudes highly suggest that barotropic/baroclinic instability of the polar night jet and/or the double-jet structure, a high-latitude feature especially in winter, is responsible for the confined wave generation. This hypothesis will be further elucidated in section 4.1.

[22] PWs tend to have propagating characteristics in the region where amplitudes are large for the 4–day wave (Figure 6). From 38 to 48 km poleward of 70° S, the phase changes from 330° to 270° approximately. According to this phase change, the vertical wavelength of the 4–day wave is about 50–60 km. The phases of 2– and 1.25–day waves change relatively more rapidly below 42 and 44 km, while barely changing above these altitudes, indicative of very long vertical wavelengths or evanescent waves [Venne and Stanford, 1982]. Since the phase information above 50 km is missing, it is difficult to estimate the vertical wavelengths of 2– and 1.25–day waves. At latitudes equatorward of 50° S where wave amplitudes become smaller, phase lines tend to become more constant and waves are likely evanescent. More detailed discussion of the global amplitude and phase structure will be given in section 4.3 with respect to the refractive index, as an indication of wave propagation characteristics.

4. Wave Sources and Dynamics

4.1. EP Flux and Instability Analysis

[23] In order to verify the hypothesis that the dominant eastward propagating PWs originate from the instability of the polar night jet and/or the double-jet structure in the winter polar stratosphere, we analyze the Eliassen-Palm flux (EP flux) and the meridional gradient of the zonal mean potential vorticity (\bar{q}_y). EP flux divergence ($\nabla \cdot F$) often corresponds to a wave generation region [Randel and Lait, 1991; Lawrence and Randel, 1996]. The EP flux and its divergence in spherical, log-pressure coordinates are determined as [Andrews *et al.*, 1987]

$$F^{(\phi)} = \rho_0 a \cos \phi \left(\bar{u}_z \bar{v}' \bar{\theta}' / \bar{\theta}_z - \bar{v}' \bar{u}' \right) \quad (1)$$

$$F^{(z)} = \rho_0 a \cos \phi \left\{ \left[f - (a \cos \phi)^{-1} (\bar{u} \cos \phi)_\phi \right] \bar{v}' \bar{\theta}' / \bar{\theta}_z - \bar{w}' \bar{u}' \right\} \quad (2)$$

$$\nabla \cdot F = (a \cos \phi)^{-1} \frac{\partial}{\partial \phi} \left(F^{(\phi)} \cos \phi \right) + \frac{\partial F^{(z)}}{\partial z} \quad (3)$$

where $F^{(\phi)}$ and $F^{(z)}$ represent the horizontal and vertical components of the EP flux; a and f are the Earth's radius and Coriolis parameter; ϕ and z are latitude and height; and u , v , and θ are zonal wind, meridional wind, and potential temperature, respectively. EP flux is calculated for each PW of interest in this paper. Quantities with primes correspond to the perturbations caused by a particular PW, which are derived from the inverse 2-D FFT that only includes the frequency and wavenumber of the designated PW. For instance, the inverse 2-D FFT is computed at frequency = 0.25 day^{-1} and wavenumber = 1 to obtain the 4–day wave perturbations as function of time and longitude. Quantities with bars are their corresponding zonal mean values. Instead of using the simplified quasi-geostrophic beta-plane forms [Andrews *et al.*, 1987, equation (3.5.6)], here we include the full terms in the EP flux calculation. We find that the terms held by the quasi-geostrophic approximation constitute the majority contribution to EP flux, similar to the result by Coy *et al.* [2003].

[24] Figure 7 illustrates the EP flux vectors (red arrows) and divergences (black contours) of the 4–day wave in July, and 2– and 1.25–day PWs in June, respectively. For the 4–day wave, a maximum $\nabla \cdot F$ of $\sim 3 \text{ m s}^{-1} \text{ d}^{-1}$ is found around 77° S at 45 km, which is very close to the location of McMurdo station (77.8° S), again making it an ideal observational site for the 4–day wave. The region with large $\nabla \cdot F$ for the 4–day wave

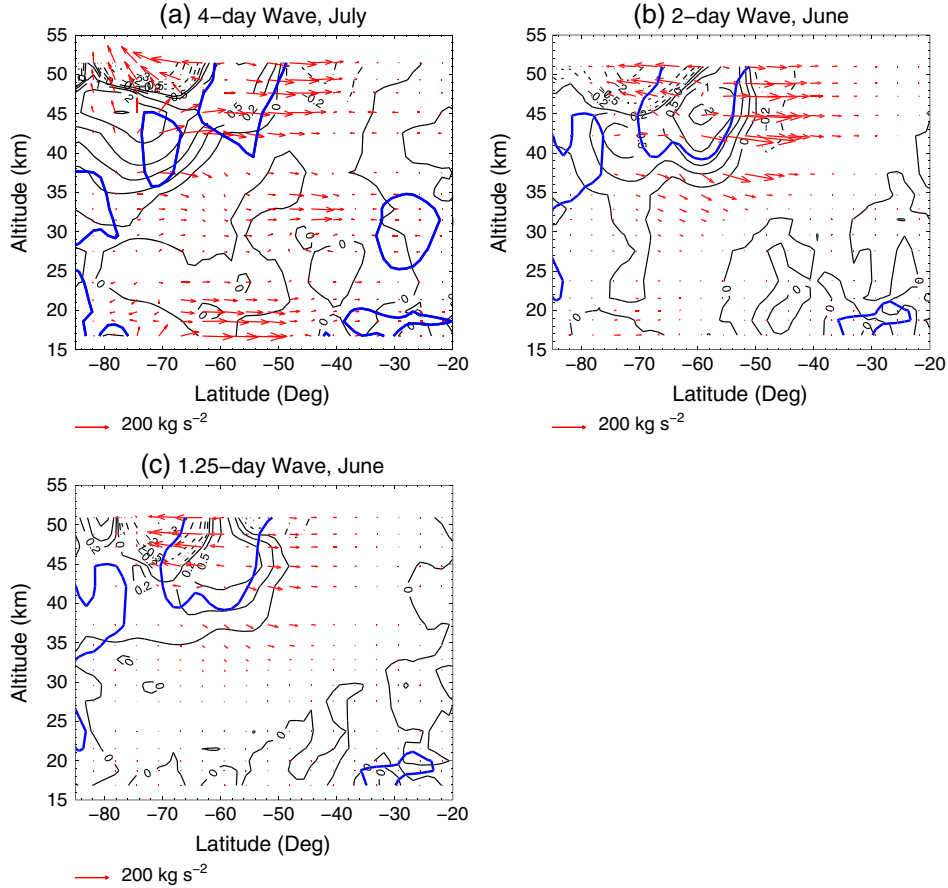


Figure 7. EP flux divergences for (a) 4-day wave in July and (b) 2-day and (c) 1.25-day waves in June 2011 represented by black contours with intervals at ± 3 , ± 2 , ± 1 , ± 0.5 , ± 0.2 , and 0. The unit is $\text{m s}^{-1} \text{d}^{-1}$. Red arrows denote EP flux vectors, where the vertical component $F^{(z)}$ has been multiplied by a viewing factor of 20. Areas enclosed by blue contours are regions with $\bar{q}_y < 0$.

extends from the pole at 30–50 km to 50°S above 40 km. For the 2- and 1.25-day PWs, the regions with large $\nabla \cdot F$ extend from the pole to 50°S above 35 km, with the maximum values of ~ 2 and $0.5 \text{ m s}^{-1} \text{d}^{-1}$ near 60°S and 45 km, respectively. For the horizontal and vertical components of EP flux (i.e., $F^{(\phi)}$ and $F^{(z)}$), the dominant quasi-geostrophic terms are respectively $\rho_0 a \cos \phi (-\bar{v}'u')$ and $\rho_0 a \cos \phi (f\bar{v}'\theta' / \bar{\theta}_z)$, proved by our scale analysis and also adopted by *Andrews et al.* [1987] and *Allen et al.* [1997]. These terms indicate that $F^{(\phi)}$ and $F^{(z)}$ are related to the momentum and heat fluxes of PWs, respectively. Due to the negative sign in $\rho_0 a \cos \phi (-\bar{v}'u')$, the equatorward EP flux $F^{(\phi)}$ denotes poleward momentum flux and vice versa. In the SH, the upward EP flux $F^{(z)}$ corresponds to poleward heat flux and vice versa due to the negative f in the SH.

[25] On the equatorward side of the region with strong $\nabla \cdot F$ (i.e., 50°S–70°S above 35 km), the momentum fluxes are normally transported to the pole denoted by the equatorward EP flux vectors, while the poleward side is characterized by equatorward momentum fluxes. This direction of the momentum fluxes is consistent with the findings by *Randel and Lait* [1991, Figures 7 and 10b]. They suggested that the 4-day wave was generated by the instability of the double-jet

structure in the upper stratosphere and mesosphere, as signified by high-latitude equatorward momentum fluxes. The conclusion that the equatorward momentum flux events appear to be consistent with instability of the double-jet structure was also supported by *Manney* [1991].

[26] Generally speaking, the heat flux is relatively small compared to the momentum flux. Consequently, the vertical components of EP flux vectors have been multiplied by 20 for viewing purposes in Figure 7. One exception to the overall small heat flux occurs in the region poleward of 70°S and above 40 km, where the 4-day PW attains the strongest $\nabla \cdot F$ and its heat flux is nonnegligible (Figure 7a). In this region, the heat flux is transported to the pole as represented by the upward EP flux vectors. This poleward direction of the heat flux is different from the results by *Randel and Lait* [1991, Figures 10b and 12b] and *Allen et al.* [1997, Figure 11], who reported an equatorward heat flux associated with the 4-day PW below 50 and 60 km, respectively. Interestingly, *Coy et al.* [2003] found equatorward heat flux below 1 hPa (similar to *Randel and Lait* [1991] as well as *Allen et al.* [1997]) but poleward heat flux above it (similar to our case). As will be discussed in section 4.2, this substantial heat transport resolved by MERRA is likely caused by the baroclinic instability of the double-jet structure and the heat flux direction is determined by the meridional gradient of background

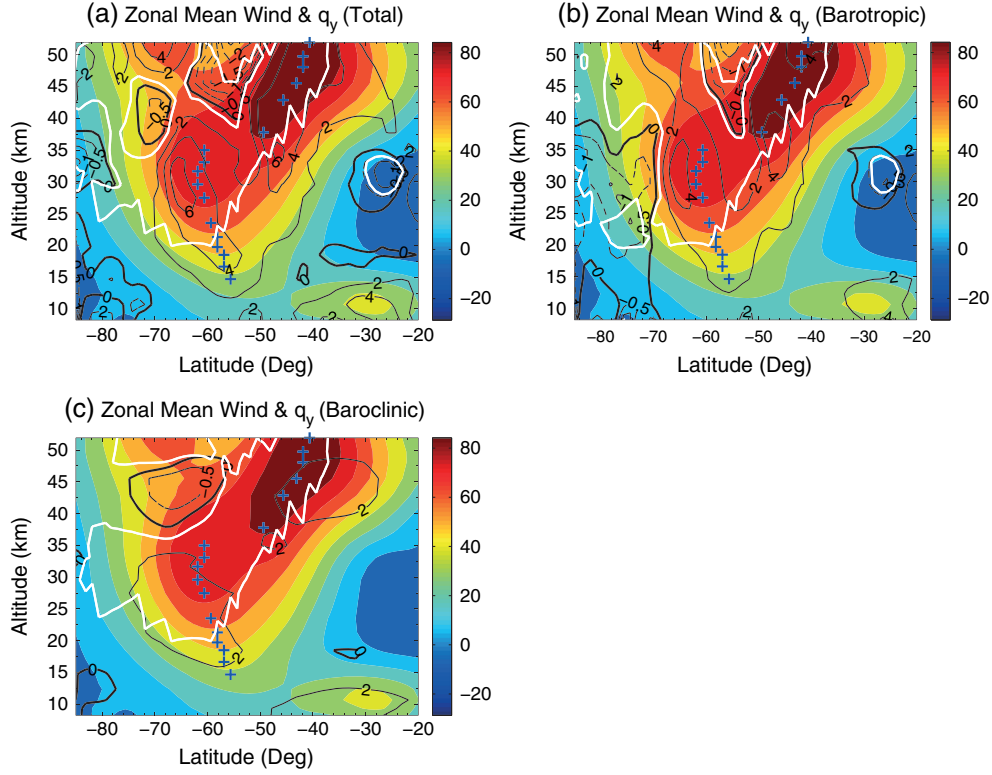


Figure 8. Zonal mean zonal winds (color contours) and the corresponding \bar{q}_y (black lines) in July 2011. The positions where $\bar{q}_y = 0$ are highlighted by thick black lines. The maximum eastward zonal mean zonal winds are denoted by blue cross symbols. The unit for the zonal wind is m s^{-1} and that for \bar{q}_y is 10^{-4} s^{-1} . Regions enclosed between white solid lines and the upper boundary of 51 km are characterized by the positive refractive indices for the 4-day wave.

temperature, which may differ between our cases and the case in *Randel and Lait* [1991] and *Allen et al.* [1997]. This difference likely accounts for the poleward heat flux in our study and the equatorward heat flux in their studies.

[27] To link the EP flux divergences with the instability of the zonal mean flow, we examine the generalized EP theorem [*Andrews et al.*, 1987]:

$$\frac{\partial A}{\partial t} + \nabla \cdot F = D + O(\alpha^3) \quad (4)$$

where F is the EP flux, A is the “wave-activity density”, and D contains the frictional and diabatic effects, which all involve mean quadratic functions of disturbance quantities. The $O(\alpha^3)$ term denotes the nonlinear wave effects and thus equals zero for linear waves. By applying the linearized potential vorticity equation, the quasi-geostrophic form of equation (4) is

$$\frac{\partial}{\partial t} \left(\frac{1}{2} \rho_0 \overline{q'^2} / \bar{q}_y \right) + \nabla \cdot F = \rho_0 \overline{Z' q'} / \bar{q}_y + O(\alpha^3) \quad (5)$$

where ρ_0 is the background density, q' is the perturbation potential vorticity associated with certain PW, and Z' is the deviation of frictional and diabatic terms from the zonal mean averages. By neglecting the external heating and friction (i.e., right-hand side (RHS) of equation (5) equals zero), for growing wave modes ($\partial \overline{q'^2} / \partial t > 0$) and positive EP flux divergence ($\nabla \cdot F > 0$), the potential vorticity gradient must

be negative ($\bar{q}_y < 0$). This comprises a necessary though not sufficient condition for the atmosphere to be unstable for wave generation [*Randel and Lait*, 1991]. The meridional gradient of the potential vorticity is calculated as [*Andrews et al.*, 1987]

$$\bar{q}_y = 2 \Omega \cos \phi - \left[\frac{1}{a \cos \phi} (\bar{u} \cos \phi) \right]_{\phi} - \frac{a}{\rho_0} \left(\frac{f^2}{N^2} \rho_0 \bar{u}_z \right)_z \quad (6)$$

where Ω is the Earth’s rotation rate and N is the buoyancy frequency. The three terms on the RHS account for the effects of the planetary vorticity gradient, as well as horizontal and vertical shears of the zonal mean zonal wind, respectively. The second and third terms on the RHS of equation (6) correspond to the barotropic and baroclinic effects of the zonal mean zonal winds, respectively. Basically, the large meridional shear of the zonal mean zonal winds will likely give rise to barotropic instability and that of the mean temperature (manifesting itself as the vertical shear of the zonal mean zonal winds under the thermal wind balance) will cause baroclinic instability. When barotropic (baroclinic) instability occurs, a small disturbance introduced into the flow will grow spontaneously and extract kinetic (potential) energy from the mean flow [*Holton*, 2004], a mechanism by which waves can be generated.

[28] Also plotted in Figure 7 are regions with negative \bar{q}_y , a necessary condition for instability. Two prominent unstable regions are identified with one between 50°S and 60°S above 40 km and the other one from 70°S to the pole below 45 km.

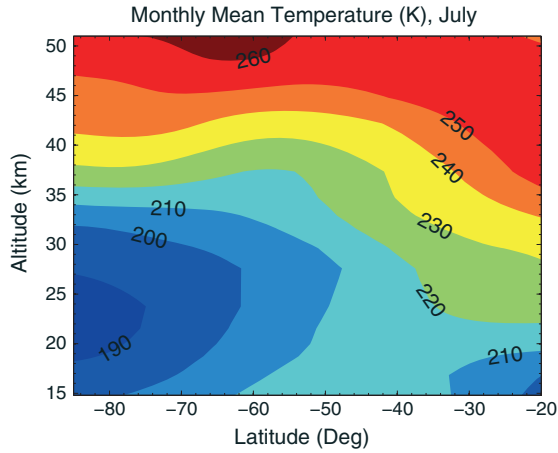


Figure 9. Monthly and zonal mean temperature in July 2011 based on the MERRA data.

The former region is in good agreement with the strong EP flux divergences of the 4-, 2-, and 1.25-day waves and the latter region coincides with the strongest 4-day wave divergence. It is worth to note that there is a possibility that the 2-day wave could be generated by the nonlinear self-interaction of the dominant 4-day wave according to the studies by *Pogoreltsev* [2001] and *Pogoreltsev et al.* [2002]. Nevertheless, the overlap between the EP flux divergences and the unstable regions strongly suggests that instability is more likely the mechanism for all these three waves. An eigenvalue analysis of the nondivergent barotropic model showed that barotropic instability in the region of negative potential vorticity gradient on the poleward side of the polar night jet can produce a wave of “4-day” variety and on the equatorward side, it will produce waves with periods of the order of a week or more [*Hartmann*, 1983]. By applying 10 years of NMC data and stability analysis, *Manney* [1991] also found that the barotropic instability caused by both the stratospheric polar night and double-jet structure can generate a 4-day wave. *Randel and Lait* [1991] further pointed out that the baroclinic instability associated with the double-jet structure is responsible for the heat flux transport. *Watanabe et al.* [2009] showed that the double-jet structure is resolved in their gravity wave resolving general circulation model (GCM) and is essential for the 4-day wave generation. Our study is supportive of the prior studies in the context of wave sources.

4.2. Structures of Jets and Background Temperature

[29] The zonal mean zonal wind is calculated using the MERRA data and shown in Figure 8 (color contours) for July 2011. The maximum winds at each altitude are highlighted by the blue cross symbols. Below ~ 35 km, the polar night jet core (noted as maximum zonal mean zonal winds on the order of $50\text{--}60\text{ m s}^{-1}$) can be found near 60°S . From 35 to 51 km, one branch of maximum winds (larger than 60 m s^{-1}) is shifted toward the equator and is centered at $40^\circ\text{S}\text{--}50^\circ\text{S}$ and the other branch with the secondary maximum winds (on the order of $40\text{--}60\text{ m s}^{-1}$) is shifted toward the pole ultimately reaching $\sim 70^\circ\text{S}$ at 50 km. As a consequence, a double-jet structure forms near the stratopause in July. This scenario is very similar to that presented by *Coy et al.* [2003], who showed that “the jet tilts strongly equatorward” with increasing altitude and there is a weak poleward secondary maximum near the stratopause (see their Figure 5a). Due to the lack of winds above 50 km in

MERRA, it is difficult (and may be also of trivial importance) to determine whether the jet core at $40^\circ\text{S}\text{--}50^\circ\text{S}$ above 35 km is the downward extension of the subtropical mesospheric jet or the equatorward displacement of the polar night jet. It is this double-peak structure that eventually matters for the barotropic/baroclinic instability.

[30] By comparing Figures 8b and 8c, we find that the unstable region at $50^\circ\text{S}\text{--}60^\circ\text{S}$ above 35 km arises largely from the barotropic instability of the double-jet structure, whereas the region near 70°S at 35–50 km results from the baroclinic instability. This structure perfectly explains the barotropic nature of the 4-, 2-, and 1.25-day PWs (i.e., characterized by large momentum flux but small heat flux) near the former region and the baroclinic nature (i.e., with significant heat flux) of the 4-day wave near the latter region (Figure 7a). The barotropic instability poleward of 70°S below 40 km can be also identified (Figure 8b). However, adding the baroclinic effect diminishes the total instability in this region, which means that the baroclinic effect of the zonal mean flow tends to offset the barotropic instability. In spite of this offset, the instability in this region is still present (Figure 8a) and likely accounts for the 4-day wave originating from the pole ($80^\circ\text{S}\text{--}50^\circ\text{S}$) below 40 km (Figure 7a). Since this region is dominated by the barotropic instability (Figure 8b), the EP flux vectors of the 4-day wave here are mainly horizontal, indicative of large momentum flux but small heat flux. The similar region (i.e., poleward of 70°S below 40 km) with instability is also discernable in *Randel and Lait* [1991], *Manney and Randel* [1993], *Allen et al.* [1997], *Lawrence and Randel* [1996], and *Watanabe et al.* [2009], while no substantial flux divergences are linked with it.

[31] As mentioned earlier in section 4.1, the poleward heat flux of the 4-day wave at $65^\circ\text{S}\text{--}80^\circ\text{S}$ above 40 km is different from the reports by *Randel and Lait* [1991] and *Allen et al.* [1997]. *Randel and Lait* [1991] stated that the nature of the baroclinic component is such that heat is transported toward the equator in the upper stratosphere (see their Figure 12b), which is downgradient to the background of the warm polar stratopause. This implies that the background temperature in the region of their interest (i.e., $50^\circ\text{S}\text{--}80^\circ\text{S}$) increases to the pole at the stratopause. A closer examination on the monthly-mean background temperature in July 2011 from the MERRA exhibits a different structure. Figure 9 shows that near the polar stratopause (> 45 km), the warmest temperature occurs at latitudes of $60^\circ\text{S}\text{--}70^\circ\text{S}$ other than the pole. Therefore, the downgradient to the background temperature is from 60°S to 70°S toward the pole, which completely matches our finding that the 4-day wave (in the region of $65^\circ\text{S}\text{--}80^\circ\text{S}$ above 40 km) has significant poleward heat flux caused by the baroclinic instability of the double-jet structure. It is suggested that the direction of heat flux is virtually determined by the background temperature distribution and it can vary from one year to another.

[32] The similar double-jet structure is seen for June 2011, except that the primary jet is more equatorward and has a wider breadth (Figure 10). This structure results in the smaller horizontal wind shear and thus smaller barotropic instability in the region poleward of 70°S below 40 km. A closer inspection of Figures 8a and 10a illustrates that the regions with instability are often accompanied by relatively weak zonal mean zonal winds, which are sandwiched by the strong winds from the jets. The numerical study by

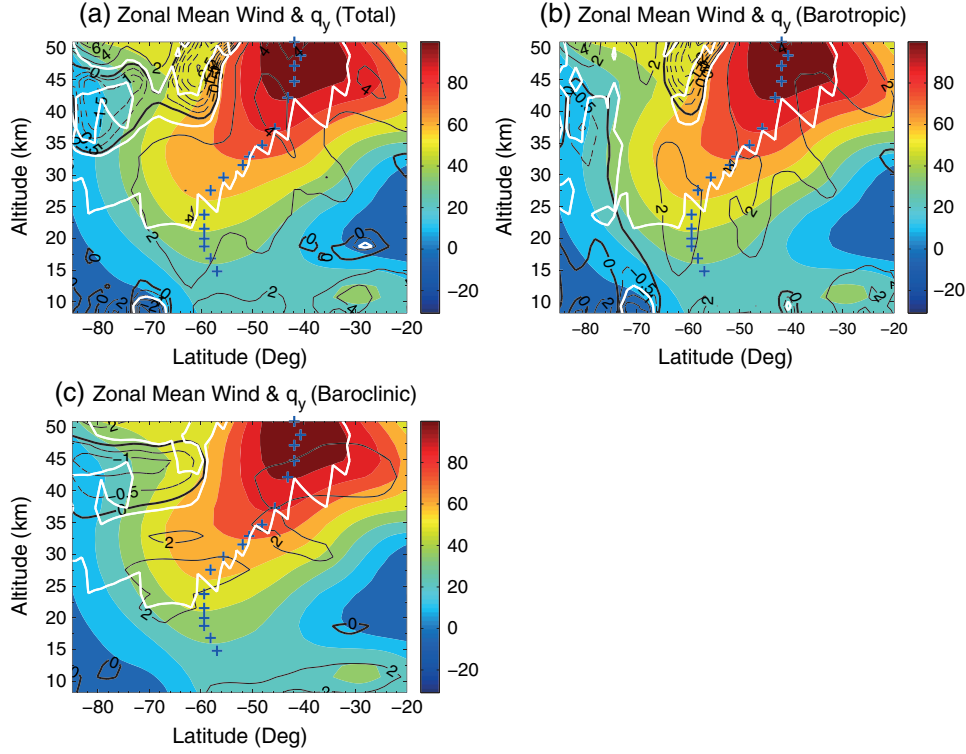


Figure 10. Same as Figure 8 except in June 2011 and the white solid lines correspond to $m^2=0$ for the 2-day PW.

Hartmann [1983] showed that the EP flux divergence region (coincident with negative \bar{q}_y) corresponds to the polar flank of the jet core and EP flux convergence (coincident with positive \bar{q}_y) corresponds to the jet core (see their Figures 11 and 12). The divergence (convergence) caused by this group of eastward propagating PWs was found to accelerate (decelerate) the zonal mean flow based on his study. The relation that EP flux divergence causes the eastward forcing (acceleration) on the mean flow and convergence causes the westward forcing (deceleration) has also been confirmed by satellite observations [Randel and Lait, 1991]. By applying this principle to our case, we find that the convergences of the PWs are directed to the jet core and divergences occur in the region between the jet cores where the zonal mean zonal winds are relatively weak. This indicates that these instability-generated PWs act to decelerate the jet core and accelerate its flanks, thus diminishing the wind shears and dragging the mean flow back to a stable status.

4.3. Wave Propagation

[33] The refractive index of the atmosphere experienced by waves is widely adopted to depict wave propagation characteristics [Liu et al., 2004; Chang et al., 2011; Yue et al., 2012]. According to Andrews et al. [1987], the square of the refractive index is calculated as

$$m^2 = \frac{\bar{q}_y}{a(\bar{u} - c)} - \left(\frac{s}{a \cos \phi} \right)^2 - \frac{f^2}{4N^2 H^2} \quad (7)$$

where \bar{q}_y is the meridional gradient of mean potential vorticity, s and c are the zonal wavenumber and zonal phase

velocity of the PW, H is the scale height, and \bar{u} is the zonal mean zonal wind. Waves are expected to propagate in regions where $m^2 > 0$ but not in regions where $m^2 < 0$ [Andrews et al., 1987]. In the region where $m^2 > 0$ and $\bar{q}_y > 0$, $\bar{u} - c$ should be positive meaning the zonal mean flow (\bar{u}) must be faster than the zonal phase speed (c) of the PWs.

[34] In Figures 8 and 10, the white line corresponds to the location where $m^2=0$ and the area flanked by the white line and upper boundary (51 km) has $m^2 > 0$. It can be seen that the region where $m^2 > 0$ is shaped by positive \bar{q}_y and relatively strong eastward zonal mean zonal wind, faster than the eastward phase speeds of the PWs. In this scenario, the PWs propagate westward with respect to the mean flow, which is a typical characteristic of Rossby wave. A closer inspection of Figures 7, 8, and 10 reveals that in the region of positive m^2 , significant wave activities are expected, while outside this region, the zonal mean zonal winds become weaker and are not preferential for the propagation of these PWs because in this situation, PWs are eastward with regard to the mean flow. This may explain our findings that the wave amplitudes become smaller and the phase lines become more constant equatorward of 45°S (Figures 5 and 6), where the PWs are likely dissipated and become evanescent because the zonal mean flow is slower than the wave phase speed resulting in $m^2 < 0$. We conclude that the PWs are generated by the jet-induced instability and propagate in the adjacent regions of the instability where the zonal mean flow is stable and moves eastward faster than the PWs. As the eastward zonal mean flow slows down when going to middle and low latitudes, it moves slower than the eastward propagating PWs, eventually preventing the further propagation of these waves.

5. Conclusions

[35] This paper reveals an assessment of the PW influences on the temperature measurements by the Fe lidar at McMurdo, Antarctica (77.8°S, 166.7°E), in the austral winter of 2011. The MERRA reanalysis data show good agreement with the lidar observations, and both data sets illustrate the temperature increases/decreases of 10–20 K within one day from 35 to 51 km at McMurdo. Both the lidar and MERRA data reveal that the significant temperature perturbations are mainly caused by the eastward propagating PWs with periods of 1–5 days. Among them, the 4–day wave with wavenumber -1 is the most dominant and the 2– and 1.25–day waves with wavenumbers -2 and -3 are also identified. The MERRA reanalysis data show these eastward propagating PWs maintain large amplitudes above 35 km and they are highly confined to high latitudes. The positive EP flux divergences of the PWs are coincident with the barotropic and baroclinic instability of the double-jet structure near the stratopause, highly suggesting that the PWs are generated by the instability of the zonal mean flow.

[36] Our findings agree with previous studies in that (1) these eastward propagating PWs are ubiquitous and long-lived in the winter stratosphere and are confined to high latitudes; (2) amongst this series of PWs associated with the “warm pool” phenomenon, the 4(5) day wave is the most dominant component; (3) the instability of the double-jet structure (at 50°S–60°S above 35 km) is responsible for the wave generation and these PWs in turn play a role to smooth out the wind shears of the zonal mean flow and reduce the instability; and (4) the barotropic/baroclinic instability at 50°S–60°S induced by the double-jet structure results in the poleward momentum flux on the equatorward side of the jet and equatorward momentum flux on the poleward side.

[37] We report several new findings in our study:

[38] 1. This is the first time that the eastward propagating PWs are found to manifest themselves in the temperature perturbations of the upper stratosphere observed by a lidar at 77.8°S, where both the 4– and 2–day PWs attain their peak amplitudes.

[39] 2. In addition to the instability at 50°S–60°S, the vertical wind shear of the jet gives rise to the baroclinic instability near 70°S and above 35 km that generates the 4–day wave.

[40] 3. The heat flux associated with the 4–day wave generated by the baroclinic instability of the jet is found to be directed from $\sim 70^\circ\text{S}$ toward the pole, rather than from the pole to lower latitudes as reported by previous studies. The direction of the heat flux transport is found to be determined by the meridional gradient of background temperature near the stratopause, which in July 2011 is different from previous studies according to the MERRA (i.e., warmer near 60°S–70°S and colder at the pole).

[41] 4. The PWs encounter difficulties in propagating toward the equator where the eastward zonal mean zonal winds become weaker and the refractive indices for the PWs become negative ($m^2 < 0$). This explains the confinement of the PWs to high latitudes ($> 50^\circ\text{S}$) and likely explains the constant phase structure of the PWs equatorward of 40°S–50°S.

[42] This study has shown that the eastward propagating PWs can induce large temperature perturbations in the upper stratosphere in the winter polar region. Similar waves have been observed to be capable of extending to the mesosphere [Garcia *et al.*, 2005] and even the lower thermosphere [Palo

et al., 2005]. It will be of great interest to study the wave propagations and their energy depositions to the mean flow if and when they break. It is also intriguing to study the dynamical and chemical responses and impacts of these PWs in the mesosphere, thermosphere, and ionosphere via direct wave modulation and/or wave-mean flow and wave-wave interactions. These puzzles will motivate our future work. In addition, it is important and valuable to validate whether current GCMs reproduce the realistic eastward propagating PWs generated by the jet instability, since the presence of these PWs is a salient feature of the winter polar dynamics in the upper stratosphere. For instance, it is expected that better simulation of the polar night jet and/or subtropical jet in the wintertime at high latitudes will lead to more realistic reproduction of these PWs. Therefore, the simulation of these PWs can help to evaluate the model performance on resolving the wintertime polar dynamics.

[43] **Acknowledgments.** We sincerely acknowledge Wentao Huang, John A. Smith, Zhangjun Wang, Cao Chen, Brendan R. Roberts, and Chester S. Gardner for their contributions to the McMurdo lidar campaign. We appreciate Adrian J. McDonald and the staff of United States Antarctic Program, McMurdo Station, Antarctica New Zealand, and Scott Base for their support. The McMurdo lidar project was supported by NSF grant ANT-0839091. X.L. sincerely acknowledges the generous support of the CIRES Visiting Fellows Program (<http://cires.colorado.edu/collaboration/fellowships/>). MERRA data used in this study have been provided by the Global Modeling and Assimilation Office (GMAO) at NASA Goddard Space Flight Center through the NASA GES DISC online archive.

References

- Allen, D. R., J. L. Stanford, L. S. Elson, E. F. Fishbein, L. Froidevaux, and J. W. Waters (1997), The 4-day wave as observed from the Upper Atmosphere Research Satellite Microwave Limb Sounder, *J. Atmos. Sci.*, *54*, 420–434, doi:10.1175/1520-0469(1997)054<0420:TDWAO>2.0.CO;2.
- Andrews, D. G., J. R. Holton, and C. B. Leovy (1987), *Middle Atmosphere Dynamics*, Academic Press, San Diego, C.A.
- Azeem, S. M. I., E. R. Talaat, G. G. Sivjee, H.-L. Liu, and R. G. Roble (2005), Observational study of the 4-day wave in the mesosphere preceding the sudden stratospheric warming events during 1995 and 2002, *Geophys. Res. Lett.*, *32*, L15804, doi:10.1029/2005GL023393.
- Baumgaertner, A. J. G., A. J. McDonald, R. E. Hibbins, D. C. Fritts, D. J. Murphy, and R. A. Vincent (2008), Short-period planetary waves in the Antarctic middle atmosphere, *J. Atmos. Sol. Terr. Phys.*, *70*, 1,336, doi:10.1016/j.jastp.2008.04.007.
- Bosilovich, M. (2013), Regional climate and variability of NASA MERRA and recent reanalyses: US summertime precipitation and temperature, *J. Appl. Meteorol. Clim.*, *52*, 1939–1951 doi:10.1175/JAMC-D-12-0291.1.
- Chang, L. C., S. E. Palo, and H.-L. Liu (2011), Short-term variability in the migrating diurnal tide caused by interactions with the quasi 2–day wave, *J. Geophys. Res.*, *116*, D12112, doi:10.1029/2010JD014996.
- Chen, C., X. Chu, A. J. McDonald, S. L. Vadas, Z. Yu, W. Fong, and X. Lu (2013), Inertia-gravity waves in Antarctica: A case study using simultaneous lidar and radar measurements at McMurdo/Scott Base (77.8°S, 166.7°E), *J. Geophys. Res. Atmos.*, *118*, 2,794–2,808, doi:10.1002/jgrd.50318.
- Chu, X., G. Papen, W. Pan, C. S. Gardner, and J. Gelbwachs (2002), Fe Boltzmann temperature lidar: Design, error analysis, and first results from the North and South poles, *Appl. Opt.*, *41*, 4,400–4,410, doi:10.1364/AO.41.004400.
- Chu, X., W. Huang, W. Fong, Z. Yu, Z. Wang, J. A. Smith, and C. S. Gardner (2011a), First lidar observations of polar mesospheric clouds and Fe temperatures at McMurdo (77.8°S, 166.7°E), Antarctica, *Geophys. Res. Lett.*, *38*, L16810, doi:10.1029/2011GL048373.
- Chu, X., Z. Yu, C. S. Gardner, C. Chen, and W. Fong (2011b), Lidar observations of neutral Fe layers and fast gravity waves in the thermosphere (110–155 km) at McMurdo (77.8°S, 166.7°E), Antarctica, *Geophys. Res. Lett.*, *38*, L23807, doi:10.1029/2011GL050016.
- Coy, L., I. Stajner, A. M. Dasilva, J. Joiner, R. B. Rood, S. Pawson, and S. J. Lin (2003), High-frequency planetary waves in the polar middle atmosphere as seen in a data assimilation system, *J. Atmos. Sci.*, *60*, 2,975, doi:10.1175/1520-0469(2003)060<2975:HPWITP>2.0.CO;2.
- Cullather, R. I., and M. Bosilovich (2012), The energy budget of the polar atmosphere in MERRA, *J. Climate*, *25*, 5–24, doi:10.1175/2011JCLI1438.1.

- Forbes, J. M. (1995), Tidal and planetary waves, in *The Upper Mesosphere and Lower Thermosphere: A Review of Experiment and Theory*, Geophys. Monogr. Ser., vol. 87, edited by R. M. Johnson and T. L. Killeen, pp. 67–87, AGU, Washington, D. C.
- Forbes, J. M., I. Y. Portnyagin, N. A. Makarov, S. E. Palo, E. G. Merzlyakov, and X. Zhang (1999), Dynamics of the lower thermosphere over South Pole from meteor radar wind measurements, *Earth Planets Space*, 51, 611–620.
- Fraser, G. J., G. Hernandez, and R. W. Smith (1993), Eastward-moving 2–4-day waves in the winter Antarctic mesosphere, *Geophys. Res. Lett.*, 20, 1,547, doi:10.1029/93GL01707.
- Garcia, R. R., R. Lieberman, J. M. Russell, and M. G. Mlynczak (2005), Large-scale waves in the mesosphere and lower thermosphere observed by SABER, *J. Atmos. Sci.*, 62, 4,384–4,399.
- Hartmann, D. L. (1983), Barotropic instability of the polar night jet stream, *J. Atmos. Sci.*, 40, 817, doi:10.1175/1520-0469(1983)040<0817:BIOTPN>2.0.CO;2.
- Holton, R. J. (2004), *An Introduction to Dynamic Meteorology*, International Geophysics Series, vol. 88, 4th ed., 535 p., Academic Press, San Diego, CA.
- Lait, L. R., and J. L. Stanford (1988), Fast, long-lived features in the polar stratosphere, *J. Atmos. Sci.*, 45, 3,800, doi:10.1175/1520-0469(1988)045<3800:FLFIT>2.0.CO;2.
- Lawrence, B. N., and W. J. Randel (1996), Variability in the mesosphere observed by the Nimbus 6 pressure modulator radiometer, *J. Geophys. Res.*, 101, 23,475, doi:10.1029/96JD01652.
- Lawrence, B. N., G. J. Fraser, R. A. Vincent, and A. Philips (1995), The 4-day wave in the Antarctic mesosphere, *J. Geophys. Res.*, 100, 18,899, doi:10.1029/95JD01168.
- Liu, H.-L., E. R. Talaat, R. G. Roble, R. S. Lieberman, D. M. Riggan, and J. H. Yee (2004), The 6.5-day wave and its seasonal variability in the middle and upper atmosphere, *J. Geophys. Res.*, 109, D21112, doi:10.1029/2004JD004795.
- Liu, H.-L., V. A. Yudin, and R. G. Roble (2013), Day-to-day ionospheric variability due to lower atmosphere perturbations, *Geophys. Res. Lett.*, 40, 665–670, doi:10.1002/grl.50125.
- Manney, G. L. (1991), The stratospheric 4-day wave in NMC data, *J. Atmos. Sci.*, 48, 1,798, doi:10.1175/1520-0469(1991)048<1798:TSDWIN>2.0.CO;2.
- Manney, G. L., and W. J. Randel (1993), Instability at the winter stratopause: A mechanism for the 4-day wave, *J. Atmos. Sci.*, 50, 3,928, doi:10.1175/15200469(1993)050<3928:IATWSA>2.0.CO;2.
- Manney, G. L., T. R. Nathan, and J. L. Stanford (1988), Barotropic stability of realistic stratospheric jets, *J. Atmos. Sci.*, 45, 2,545–2,555, doi:10.1175/1520-0469(1988)045<2545:BSORSJ>2.0.CO;2.
- Manney, G. L., Y. J. Orsolini, H. C. Pumphrey, and A. E. Roche (1998), The 4-day wave and transport of UARS tracers in the austral polar vortex, *J. Atmos. Sci.*, 55, 3,456, doi:10.1175/1520-0469(1998)055<3456:TDWATO>2.0.CO;2.
- Merzlyakov, E. G., and D. V. Pancheva (2007), The 1.5–5-day eastward waves in the upper stratosphere mesosphere as observed by the Esrange meteor radar and the SABER instrument, *J. Atmos. Sol. Terr. Phys.*, 69, 2102, doi:10.1016/j.jastp.2007.07.002.
- Palo, S. E., Y. I. Portnyagin, J. M. Forbes, N. A. Makarov, and E. G. Merzlyakov (1998), Transient eastward propagating long-period waves observed over the south pole, *Ann. Geophys.*, 16, 1,486, doi:10.1007/s00585-998-1486-7.
- Palo, S. E., J. M. Forbes, X. Zhang, J. M. Russell III, C. J. Mertens, M. G. Mlynczak, G. B. Burns, P. J. Espy, and T. D. Kawahara (2005), Planetary wave coupling from the stratosphere to the thermosphere during the 2002 Southern Hemisphere pre-stratwam period, *Geophys. Res. Lett.*, 32, L23809, doi:10.1029/2005GL024298.
- Pogoreltsev, A. I. (2001), Numerical simulation of secondary planetary waves arising from the nonlinear interaction of the normal atmospheric modes, *Phys. Chem. Earth C*, 26, 395–403.
- Pogoreltsev, A. I., I. N. Fedulina, N. J. Mitchell, H. G. Muller, Y. Luo, C. E. Meek, and A. H. Manson (2002), Global free oscillations of the atmosphere and secondary planetary waves in the mesosphere and lower thermosphere region during August/September time conditions, *J. Geophys. Res.*, 107(D24), 4799, doi:10.1029/2001JD001535.
- Prata, A. J. (1984), The 4-day wave, *J. Atmos. Sci.*, 41, 150, doi:10.1175/1520-0469(1984)041<0150:TDW>2.0.CO;2.
- Randel, W. J., and L. R. Lait (1991), Dynamics of the 4-day wave in the southern hemisphere polar stratosphere, *J. Atmos. Sci.*, 48, 2,496, doi:10.1175/1520-0469(1991)048<2496:DOTDWI>2.0.CO;2.
- Rienecker, M. M., et al. (2011), MERRA: NASA's Modern-Era Retrospective Analysis for Research and Applications, *J. Climate*, 24, 3,624–3,648.
- Sakazaki, T., M. Fujiwara, X. Zhang, M. E. Hagan, and J. M. Forbes (2012), Diurnal tides from the troposphere to the lower mesosphere as deduced from TIMED/SABER satellite data and six global reanalysis data sets, *J. Geophys. Res.*, 117, D13108, doi:10.1029/2011JD017117.
- Sandford, D. J., M. J. Schwartz, and N. J. Mitchell (2008), The wintertime two-day wave in the polar stratosphere, mesosphere and lower thermosphere, *Atmos. Chem. Phys.*, 8, 749.
- Scargle, J. D. (1982), Studies in astronomical time series analysis. II. Statistical aspects of spectral analysis of unevenly spaced data, *Astrophys. J.*, 263, 835–853.
- Venne, D. E., and J. L. Stanford (1979), Observation of a 4-day temperature wave in the polar winter stratosphere, *J. Atmos. Sci.*, 36, 2,016–2,019, doi:10.1175/1520-0469(1979)036<2016:OOATWI>2.0.CO;2.
- Venne, D. E., and J. L. Stanford (1982), An observational study of high-latitude stratospheric planetary waves in winter, *J. Atmos. Sci.*, 39, 1,026–1,034, doi:10.1175/1520-0469(1982)039<1026:AOSOHL>2.0.CO;2.
- Watanabe, S., Y. Tomikawa, K. Sato, Y. Kawatani, K. Miyazaki, and M. Takahashi (2009), Simulation of the eastward 4-day wave in the Antarctic winter mesosphere using a gravity wave resolving general circulation model, *J. Geophys. Res.*, 114, D16111, doi:10.1029/2008JD011636.
- Yu, Z., X. Chu, W. Huang, W. Fong, and B. R. Roberts (2012), Diurnal variations of the Fe layer in the mesosphere and lower thermosphere: Four season variability and solar effects on the layer bottomside at McMurdo (77.8°S, 166.7°E), Antarctica, *J. Geophys. Res.*, 117, D22303, doi:10.1029/2012JD018079.
- Yue, J., H.-L. Liu, and L. C. Chang (2012), Numerical investigation of the quasi 2–day wave in the mesosphere and lower thermosphere, *J. Geophys. Res.*, 117, D05111, doi:10.1029/2011JD016574.